University of Wollongong
Research Online

Australian Institute for Innovative Materials - Papers | Australian Institute for Innovative Materials

1-1-2016

Engineering hierarchical hollow nickel sulfide spheres for high-performance sodium storage

Dan Zhang
University of Wollongong, Zhejiang University, dz966@uowmail.edu.au

Wenping Sun
University of Wollongong, wenping@uow.edu.au

Yu Zhang
Nanyang Technological University, University of Wollongong, azhang@uow.edu.au

Yuhai Dou
University of Wollongong, yd930@uowmail.edu.au

Yinzhu Jiang
Chinese Academy of Science, Zhejiang University

See next page for additional authors

Follow this and additional works at: https://ro.uow.edu.au/aiimpapers

 Part of the Engineering Commons, and the Physical Sciences and Mathematics Commons

Recommended Citation

Zhang, Dan; Sun, Wenping; Zhang, Yu; Dou, Yuhai; Jiang, Yinzhu; and Dou, Shi Xue, "Engineering hierarchical hollow nickel sulfide spheres for high-performance sodium storage" (2016). *Australian Institute for Innovative Materials - Papers*. 2289.
https://ro.uow.edu.au/aiimpapers/2289

Research Online is the open access institutional repository for the University of Wollongong. For further information contact the UOW Library: research-pubs@uow.edu.au

Engineering hierarchical hollow nickel sulfide spheres for high-performance sodium storage

Abstract

Sodium-ion batteries (SIBs) are considered as promising alternatives to lithium-ion batteries (LIBs) for energy storage due to the abundance of sodium, especially for grid distribution systems. The practical implementation of SIBs, however, is severely hindered by their low energy density and poor cycling stability due to the poor electrochemical performance of the existing electrodes. Here, to achieve high-capacity and durable sodium storage with good rate capability, hierarchical hollow NiS spheres with porous shells composed of nanoparticles are designed and synthesized by tuning the reaction parameters. The formation mechanism of this unique structure is systematically investigated, which is clearly revealed to be Ostwald ripening mechanism on the basis of the time-dependent morphology evolution. The hierarchical hollow structure provides sufficient electrode/electrolyte contact, shortened Na+ diffusion pathways, and high strain-tolerance capability. The hollow NiS spheres deliver high reversible capacity (683.8 mAh g−1 at 0.1 A g−1), excellent rate capability (337.4 mAh g−1 at 5 A g−1), and good cycling stability (499.9 mAh g−1 with 73% retention after 50 cycles at 0.1 A g−1).

Keywords

high-performance, spheres, sulfide, nickel, hollow, hierarchical, storage, engineering, sodium

Disciplines

Engineering | Physical Sciences and Mathematics

Publication Details

Zhang, D., Sun, W., Zhang, Y., Dou, Y., Jiang, Y. & Dou, S. Xue. (2016). Engineering hierarchical hollow nickel sulfide spheres for high-performance sodium storage. Advanced Functional Materials, 26 7479-7485.

Authors

Dan Zhang, Wenping Sun, Yu Zhang, Yuhai Dou, Yinzhu Jiang, and Shi Xue Dou

This journal article is available at Research Online: https://ro.uow.edu.au/aiimpapers/2289

DOI: 10.1002/
Article type: Full paper

Engineering Hierarchical Hollow Nickel Sulfide Spheres for High-Performance Sodium Storage

Dan Zhang, Wenping Sun, Yu Zhang, Yuhai Dou, Yinzhu Jiang*, Shi Xue Dou*

D. Zhang, Dr. W. Sun, Y. Zhang, Y. Dou, Prof. S. X. Dou
Institute for Superconducting and Electronic Materials, University of Wollongong, Wollongong, NSW 2522, Australia
E-mail address: wenping@uow.edu.au (W. Sun)
D. Zhang, Prof. Y. Jiang
State Key Laboratory of Silicon Materials, Key Laboratory of Advanced Materials and Applications for Batteries of Zhejiang Province and Department of Materials Science and Engineering, Zhejiang University, Hangzhou, Zhejiang 310027, P. R. China
E-mail address: yzjiang@zju.edu.cn (Y. Jiang)

Keywords: Nickel sulfide; hollow structure; anode; sodium-ion batteries

Abstract: Sodium-ion batteries (SIBs) are considered as promising alternatives to lithium-ion batteries (LIBs) for energy storage due to the abundance of sodium, especially for grid distribution systems. The practical implementation of SIBs, however, is severely hindered by their low energy density and poor cycling stability due to the poor electrochemical performance of the existing electrodes. Herein, to achieve high-capacity and durable sodium storage with good rate capability, hierarchical hollow NiS spheres with porous shells composed of nanoparticles were designed and synthesized by tuning the reaction parameters. The formation mechanism of this unique structure is systematically investigated, which is clearly revealed to be Ostwald ripening mechanism on the basis of the time-dependent morphology evolution. The hierarchical hollow structure provides sufficient electrode/electrolyte contact, shortened Na^+ diffusion pathways, and high strain-tolerance capability. The hollow NiS spheres deliver high reversible capacity (683.8 mAh g^{-1} at 0.1 A g^{-1}), excellent rate capability (337.4 mAh g^{-1} at 5 A g^{-1}), and good cycling stability (499.9 mAh g^{-1} with 73% retention after 50 cycles at 0.1 A g^{-1}).

1. Introduction

Sodium-ion batteries (SIBs) have attracted ever-increasing attention lately as a promising alternative to lithium-ion batteries (LIBs) for energy storage[1-5]. Due to the abundance of sodium resources, SIBs are more attractive for grid distribution systems. To date, the study of cathode materials for SIBs, such as various layered oxides[6-10], polyanionic compounds[11-14], and Prussian-blue-based materials[15-17], is very progressive[18]. Nevertheless, developing durable and high-capacity anode materials is still a major issue[19]. Even though tremendous efforts have been devoted to developing anode materials for SIBs, including carbonaceous materials[20-25], transition metal oxides[26-30], intermetallic compounds[31-34], *etc.*, most of these reported materials still exhibit low reversible capacities or poor cycle life. Notably, their sodium storage performance is very inferior as compared with lithium storage, which might be induced by the sluggish sodiation/desodiation reaction kinetics. Therefore, it is highly desirable and greatly challenging to develop a robust anode material with high specific capacity and good cycling stability for sodium storage.

Similar to transition metal oxides, most metal sulphides are capable of storing lithium or sodium via the conversion reaction or a combined conversion-alloying reaction, and they possess promisingly high theoretical capacities[35-39]. Basically, metal sulphides exhibit higher electrical conductivity than metal oxides, and this unique property is critical for accelerating reaction kinetics, especially for sodiation/desodiation reactions [40, 41]. In terms of lithium storage, much encouraging progress on metal sulphide anodes has been reported [42-44]. Recently, several metal sulfides (SnS_2[35, 45-47], MoS_2[48-50], CoS_x(x=1,2)[36, 51-53] and FeS_2[54]) have been experimentally investigated as anode materials for SIBs and have shown very impressive sodium storage performances. It should also be mentioned, however, that metal sulfides still suffer from huge volume changes caused by the conversion reaction during the lithiation/delithiation or sodiation/desodiation reactions[55-57]. This would lead to electrode cracking, pulverization, and disconnection from current collectors over the course of cycling, eventually resulting in rapid capacity fading.

To mitigate the rapid capacity fading induced by the large volume expansion, developing hierarchical and hollow structures, with nanosized building blocks, a porous shell, and an interior cavity has been demonstrated to be a very effective approach[40, 58-61]. On the one hand, the porous shells and hollow structures provide enough spaces to buffer the strain induced by the volumetric expansion/shrinkage during repeated insertion/extraction of Li^+ or Na^+. In addition, the hollow spheres are loosely stacked, which can further accommodate volumetric change, leading to much enhanced cycling stability. On the other hand, the hollow structures with porous shells provide highly accessible surface areas for sufficient electrode/electrolyte contact, and the nanoscale building blocks significantly shorten the Li^+/Na^+ diffusion pathways for enhanced reaction kinetics, which is very crucial for delivering high capacity and excellent rate capability.

Among the various metal sulfides, nickel sulphide stands out as a popular electrode material for LIBs due to its abundance, high electronic conductivity, and high theoretical capacity[62, 63]. NiS and NiS_2 are relatively easier to be prepared compared to other nickel sulphide with different Ni/S ratio (such as Ni_3S_4 and Ni_3S_2, *etc*.) [64]. NiS_2 nanoparticles and *β*-NiS nanorods with rhombohedral structure have been reported as anodes for SIBs, but both showed inferior performances [65]. Herein, hierarchical hollow *α*-NiS spheres with porous shells constructed from nanoparticles were successfully developed as an anode for SIBs via a facile refluxing method. The formation mechanism of the hierarchical hollow structures was revealed to be the Ostwald ripening mechanism, according to the time-dependent morphology evolution. The hierarchical hollow NiS spheres deliver high reversible capacity (683.8 mAh g^{-1} at 0.1 A g^{-1}), excellent rate capability (337.4 mAh g^{-1} at 5 A g^{-1}), and good cycling stability (499.9 mAh g^{-1} with 73% retention after 50 cycles at 0.1 A g^{-1}).

2. Results and discussion

The NiS morphology exhibits significant dependence on the reaction temperature, as evidenced by field emission scanning electron microscopy (FESEM) and transmission

electron microscopy (TEM) observations. FESEM (**Figure 1**a) and TEM images (Figure 1e) show that the product obtained at 180 °C (designated as NS180) consists of a large quantity of solid spheres with sizes in the range of 100-300 nm. The surfaces of the solid spheres become rougher and are decorated with very small nanoparticles when the temperature is increased to 200 °C (NS200, Figure 1b and 1f). The nanoparticles might come from the reprecipitation of the dissolved NiS[67]. An interesting structural evolution from solid spheres to porous spheres is observed when the reaction is carried out at the higher temperature of 220 °C (NS220, Figure 1c). From the enlarged FESEM image of a cracked sphere (inset of Figure 1c), the yolk-shell structure is clearly observed, and both the solid core and porous shell are constructed from nanoparticles. The TEM image (Figure 1g) exhibits an intensive contrast between the black core and the bright surrounding area, further confirming the formation of the yolk/shell structure. Meanwhile, it can be also seen that some perfect hollow spheres have been formed. Most of the spheres present the hollow structure with a porous shell when the reaction temperature is further increased to 240 °C (for sample NS240), as shown in Figure 1d and 1h. It can be seen that the hierarchical hollow spheres have an average diameter of 220 nm. It should be mentioned that the sphere size shows no obvious dependence on the reaction temperature. Apart from the morphology evolution, the crystallinity of the product also varies obviously with the reaction temperature. The X-ray diffraction (XRD) pattern (Figure S1, Supporting Information) shows that NS180 and NS200 are not crystallized. The halo rings in their selected area electron diffraction (SAED) patterns (the insets of Figure 1e, f) confirm their amorphous nature. The X-ray photoelectron spectroscopy (XPS) spectra of Ni and S (Figure S2, Supporting Information) for NS180 comfirm the existence of Ni^{2+} and S^{2-}, which suggesting the formation of NiS. The product is gradually crystallized with increasing reaction temperature. Distinct diffraction peaks appear when the temperature is raised up to 220 and 240 °C; meanwhile, the SAED patterns of NS220 (inset of Figure 1g) and NS240 (inset of Figure 1h) show distinct diffraction rings, suggesting good crystallinity. The XRD

diffraction peaks of NS220 and NS240 can be indexed to hexagonal NiS (JCPDS card No. 75-0613). Similarly to NS220, the SAED pattern of NS240 can be indexed to the (100), (101), (102), and (110) planes of hexagonal NiS from inside to outside (the inset of Figure 1h). Clearly, the reaction temperature plays a vital role in NiS synthesis in terms of morphology and crystallinity.

Further characterization of NS240 was conducted to prove the successful synthesis of hierarchical hollow NiS spheres. **Figure 2**a shows a high resolution TEM (HRTEM) image of a typical hollow NiS sphere. The electron signal intensity measurement on the cross-section of the hollow sphere (Figure 2b) shows more counts thorough the inner part than the shell layer, which indicates the vacant inner space. On the basis of the energy dispersive X-ray spectroscopy (EDX) result (Figure 2c), only the Ni and S belonging to the as-prepared sample are detected; meanwhile, the atomic ratio of Ni and S is determined to be 1:1.1, very close to the theoretical value. The elemental mapping images of NS240 (Figure 2d and 2e) show that both Ni and S are distributed homogenously throughout the inner cavity and concentrated in the shell layer, which is more solid evidence for validating the hollow structure. As can be seen from the HRTEM image of NS240 (Figure 2f), crystallized nanograins with different crystallographic orientations can be observed. The lattice spacing of 2.54 Å can be assigned to the (101) crystal planes of hexagonal NiS. Figure 2g and 2h present high-resolution XPS spectra of Ni and S for NS240. The peaks at 855.7 and 872.9 eV correspond to Ni $2p_{3/2}$ and $2p_{1/2}$ of Ni^{2+}, respectively, while the peak at 161.5 eV can be assigned to S $2p_{3/2}$.

To further investigate the formation mechanism of the hierarchical hollow NiS spheres, time-dependent experiments were carried out at 220 °C. Nanoparticles with smooth surfaces were collected after reaction for 1 min at 220 °C (**Figure 3**a). The TEM image (Figure 3e) shows the solid nature of these particles, with diameters in the range of 200-250 nm. The particles are amorphous, as revealed by both the SAED pattern (the inset of Figure 3e) and the XRD analysis (Figure S2, Supporting Information). When the reaction time is extended to 10

min, solid spheres with rough surfaces are formed, and the surfaces are decorated with very small nanoparticles, which is similar to the case of NS200 (Figure 3b). Both the SAED (inset of Figure 3f) and XRD patterns (Figure S2, Supporting Information) indicate that the as-prepared solid spheres are amorphous, although the HRTEM image (Figure S3a, Supporting information) shows some crystallized nanocrystals, with a clear lattice spacing of 1.73 Å, which is assigned to the (110) planes of hexagonal NiS. On further prolonging the reaction time to 30 min, the products are transformed into yolk-shell spheres (Figure 3c). Moreover, in addition to the thin shell and small solid core, a distinct void can be observed from the TEM image (Figure 3g). These yolk-shell spheres are well-crystallized, as indicated by their XRD pattern (Figure S2, Supporting information), as well as the clear diffraction ring in the SAED pattern (inset of Figure 3g). As shown in the HRTEM image (Figure S3b, Supporting information), the lattice fringe spacings of 2.01, 2.54 and 3.04 Å correspond to the (102), (101), and (100) crystal planes of NiS, respectively. As the reaction time increases to 4 h, hierarchical hollow spheres with nanoparticles as building blocks are obtained (Figure 3d and 3h), which reveals the disappearance of the solid cores and conversion into perfect hollow structures. Meanwhile, the crystallinity of the products is further increased, which can be proved by the more intense diffraction peaks in the XRD pattern (Figure S2, Supporting information). The (101) plane lattice spacing of 2.54 Å can be resolved from the HRTEM image (Figure S3c, Supporting information). Time-dependent experiments were also carried out at 240 °C, and similar morphology evolution was observed. As revealed in Figure S4 (Supporting information), yolk-shell spheres are formed after reaction at 240 °C for only 5 min, and hollow spheres are formed after reaction for 2 h. Due to the accelerated reaction kinetics at 240 °C, the formation of the yolk-shell and hollow structures is much more rapid.

Based on the above temperature-dependent and time-dependent morphology evolution, we can deduce that the formation of the hierarchical hollow NiS spheres follows the Ostwald ripening mechanism (**Figure 4**). In the beginning, the Ni ions adsorb onto the surfaces of

nanosized 1,3,4-thiadiazole-2,5-dithiol (DMCT) micelles in triethylene glycol via the coordination of functional groups, such as -SH, on the micelle surface, which leads to the formation of NiS nanocrystallites. Then, these nanocrystallites randomly aggregate into solid spheres, driven by the minimization of total interfacial energy, although the solid NiS spheres are still poorly crystallized due to the rapid nucleation and growth. After that, surface crystallites begin to grow at the expense of the others nearby due to the higher interfacial energy and easier solubility of the inner nanocystallites. As a result, an interior space is generated underneath, leading to the formation of the yolk-shell structure. Finally, the hierarchical hollow structure is generated with complete depletion of the yolk inside, which shows improved crystallinity and is constructed from numerous nanoparticles.

As a proof-of-concept demonstration, the sodium storage performance of NS240 was evaluated in half cells. **Figure 5**a shows representative cyclic voltammograms (CVs) of the initial four cycles at a scan rate of 0.1 mV s^{-1} between 0.01 and 3.0 V (vs. Na/Na^+). In the first cycle, the cathodic scan shows one broad and intense reduction peak ranging from 0.4 to 1.5 V, which could be attributed to the formation of the solid electrolyte interphase (SEI) film and a sequence of reduction reactions of the active material. Ex-situ HRTEM of the NiS anode at different sodiation/desodiation states was conducted to explore the sodium storage mechanism. As shown in Figure S5a (Supporting information), lattice fringes with interplanar distances of ~2.85 Å and 3.30 Å, corresponding to $(10\bar{1})$ crystal planes of Ni_3S_2 and (200) crystal planes of Na_2S, appear when the cell is discharged to 1.0 V, indicating the formation of Ni_3S_2. As the cell is discharged to 0.01 V, the lattice spacing of ~3.30 Å and ~2.29 Å (Figure S5b and c, Supporting information) corresponds to (200) and (202) planes of Na_2S, respectively. The lattice spacing of ~1.77 Å and ~2.03 Å can be assigned to (200) and (111) planes of Ni, accordingly. A two-step reduction is proposed in Equations (1) and (2), which is in accordance with previous reports on the conversion reaction of NiS as anode material for LIBs[62, 63, 68, 69].

$3NiS + 2\ Na^+ + 2e^- \rightarrow Ni_3S_2 + Na_2S$ (1)

$Ni_3S_2 + 4\ Na^+ + 4e^- \leftrightarrows 3Ni + 2\ Na_2S$ (2)

When the cell is fully charged to 3.0 V, lattice spacing of 2.85 Å, which can be assigned to the (10 $\bar{1}$) crystal planes of Ni_3S_2, is observed (Figure S5d, Supporting information). Correspondingly, the strong oxidation peak at ~1.6 V in the anodic scans should result from the extraction of sodium ions from Na_2S and the reconstitution of Ni_3S_2. The reduction peak splits into two separate peaks and shifts to higher potential (~ 0.7 V and ~ 1.2 V) in the subsequent cycles, indicating the two-step sodiation reactions of Ni_3S_2 (Equation (2)). After the second cycle, the CV profiles are well preserved, indicating good reversibility of the sodiation/desodiation reactions after the first activation cycle.

Galvanostatic charge/discharge curves of NS240, with a cut-off voltage of 0.01-3.0 V at a current density of 0.1 A g^{-1}, are displayed in Figure 5b. The first cycle delivers a discharge (sodiation) capacity of 1049.3 mAh g^{-1}, and 54.7% of the inserted Na can be reversibly desodiated, giving a charge capacity of 574.5 mAh g^{-1}. The irreversible capacity in the first cycle is in great part due to the formation of the SEI layer on the electrode surface and electrolyte decomposition[70]. In the first discharge curve, there are three long slopes between 0.4 and 1.5 V, indicating the presence of multiple-step sodiation reactions in the initial NiS electrode. The following discharge curves have two notable slopes at ~ 0.5 and ~ 1.0 V, corresponding to the two-step transformation of Ni_3S_2 to Ni. During all the charge processes, the desodiation reaction is represented by a plateau at around 1.7 V. The voltage hysteresis of around 0.7 V from the 2nd charge-discharge process is a typical characteristic for conversion-type reaction[39]. All of these voltage profiles are in good agreement with the CV results in Figure 5a. Furthermore, it should be noted that the voltage profiles of both sodiation and desodiation processes are reproducible from cycles 1 to 10, indicating the stable structure of the hierarchical hollow NiS spheres and their excellent electrochemical reversibility during cycling.

Figure 5c shows the cycling performance of NS240 at a current density of 100 mA g^{-1}. The NS240 (hollow spheres) shows dramatically enhanced cycling performance as compared with NS200 (solid particles). NS240 still delivers the remarkable reversible capacity of 499.9 mAh g^{-1} after 50 cycles, which corresponds to 73% of the initial reversible discharge capacity (683.8 mAh g^{-1}). Even when cycled at a higher current density of 500 mA g^{-1}, a reversible capacity of 283 mAh g^{-1} is still sustained after 50 cycles (Figure S6, Supporting information). Severe and continuous capacity decay is observed for the NS200 electrode, however, and the charge capacity deteriorates to 258.1 mAh g^{-1}, with only 40.2% retention during the 50^{th} cycle. The coulombic efficiency of both electrodes increase over cycling and rise up to ca. 95% (Figure S7, Supporting information), which can be ascribed to the gradual passivation of the electrode[71]. Furthermore, NS200 electrode undergoes much more severe voltage hysteresis induced by the more sluggish conversion-reaction kinetcis during cycling, as revealed from the charge/discharge curves (Figure S8, Supporting information). As can be seen from the ex-situ SEM images of electrodes after cycling test (Figure S9, Supporting information), the electrode structure integrity of NS240 electrode is kept very well without any obvious cracks after 20 cycles. In contrast, significant cracks can be observed after the first cycle and get serious over cycling for NS200. As discussed previously, the unique hollow structure is beneficial for accommodating volume change during sodiation/desodiation reactions and should definitely play a key role in the improved cycling stability of NS240. It is notable that the promising cycling performance of NS240 is acquired without any functional coating by carbon or other materials that can effectively tolerate the massive volume changes and alleviate the stress during the conversion reaction. Therefore, we can anticipate that further improvement of the cycling performance could be achieved by employing carbon coating or some other surface/microstructure modification strategies.

Figure 5d shows the rate performance of the NS240 and NS200 electrodes. The NS240 electrode delivers reversible charge capacity of 511.5, 501.5, 485.2, 459.6, and 426.3 mAh g^{-}

^{1} at current densities of 0.2, 0.3, 0.5, 1, and 2 A g^{-1}, respectively. Even when the current density is increased to 3 and 5 A g^{-1}, the capacity shows high retention of 393.0 and 337.4 mAh g^{-1}, respectively. When the current density is reset to 0.1 A g^{-1}, a relatively high charge capacity of 406.9 mAh g^{-1} can still be achieved, which also confirms the good stability of NS240. The discharge/charge profiles are well kept at high rates (Figure S10, Supporting information). Notably, the overpotential of the cell does not increase too much with increasing current density, confirming the good rate performance of the cell. NS240 shows superior cycling stability and rate capability over other reported nickel sulphides (Table S1). It has to be mentioned that the performance of NS240 is even better than those nickel sulphides modified with reduced graphene oxide. In stark contrast, the capacity of the NS200 electrode drops promptly from 428.8 to 98.5 mAh g^{-1} when the current density increases from 0.1 to 5 A g^{-1}, indicating the poor rate performance of the solid NiS spheres. The good rate performance of NS240 can be attributed to the hollow structure with its porous shell. In addition to accommodating volume change, the interior cavity serves as a reservoir of electrolyte and provides more contact area between the electrode and electrolyte. The porous shell composed of nanoparticles significantly helps to enhance electrolyte penetration, ion diffusion, and charge transfer, eventually resulting in fast sodiation/desodiation reaction kinetics.

3. Conclusions

In summary, we have successfully developed a facile refluxing method for synthesizing porous NiS spheres with a unique hierarchical hollow structure. A possible Ostwald ripening mechanism is proposed to explain the structural evolution from solid particles to yolk-shell hollow spheres and then finally to perfect hollow spheres. The electrochemical behaviour of the hierarchical hollow NiS spheres for sodium storage was evaluated. Excellent cycling stability (499.9 mAh g^{-1} with 73% retention after 50 cycles at 0.1 A g^{-1}) and rate capability (337.4 mAh g^{-1} at 5 A g^{-1}) were achieved, based on the hierarchical hollow structure, which

ensures high Na ion accessibility and strong structural integrity. In addition to sodium storage, such hierarchical hollow NiS spheres are anticipated to have potential applications in other energy storage and conversion fields (e.g. LIBs, supercapacitors, and catalysis).

4. Experimental Section

Synthesis of hierarchical hollow NiS spheres: In a typical synthesis, 0.8 mM $NiCl_2$ (Alfa) and 0.8 mM 1,3,4-thiadiazole-2,5-dithiol (DMCT) (Sigma-Aldrich, 98%) were added into 20 mL triethylene glycol (Sigma) in a three-neck flask to form a suspension. High purity argon gas was then introduced to purge the suspension for 20 min under magnetic stirring. After that, the suspension was quickly heated to 180, 200, 220, or 240 °C under stirring and held at that temperature for a 2 h dwell time. During heating, $NiCl_2$ and DMCT were completely dissolved, forming a transparent yellow solution. Subsequently, a black product was gradually formed with time. The products were finally collected by centrifugation, washed with ethanol for 5 times, and dried at 80 °C overnight in a vacuum oven. The products synthesized at 180, 200, 220 and 240 °C are denoted as NS180, NS200, NS220 and NS240, respectively. To further explore the formation mechanism of the hierarchical hollow NiS submicron spheres, we studied the morphology evolution by varying the reaction time (1 min, 10 min, 30 min, and 2 h) at 220 °C.

Characterization: The morphology of the as-prepared products was observed by a JEOL JSM-7500FA field-emission scanning electron microscope (FESEM) and a JEOL 2010 transmission electron microscope (TEM). The phase and surface chemical state were determined by X-ray diffraction (XRD, MMA GBC, Australia) and X-ray photoelectron spectroscopy (XPS, Phoibos 100 Analyser, SPECS, Germany; Al K_α X-rays), respectively. Scanning TEM (STEM) images were acquired on a probe-corrected JEOL ARM200F operated at 200 kV equipped with a cold field emission gun, a high resolution pole-piece, and a Centurio energy dispersive spectroscopy (EDS) detector. Images and EDS maps were acquired at a probe current of 90 pA.

Electrochemical Measurements: As a proof-of-concept demonstration, the sodium storage performances of NS200 and NS240 were evaluated. The NiS powders were thoroughly mixed with carbon nanotubes (CNTs) and poly(vinyl difluoride) (PVDF) in a weight ratio of 7:2:1 in N-methylpyrrolidone solvent to form a homogeneous slurry. The cell working electrodes were prepared by painting the slurry on copper foil, followed by vacuum drying at 80 °C overnight. The mass loading of the electrode is around 0.6 mg cm^{-2}. The coin-type half-cells were assembled in an Ar-filled glove box with both H_2O and O_2 levels less than 1 ppm. Metallic Na was employed as the counter/reference electrode, and Whatman GF/D microfiber filter paper was used as the separator. 1 M $NaClO_4$ dissolved in propylene carbonate (PC) with 5% fluoroethylene carbonate (FEC) additive was chosen as the electrolyte. Galvanostatic charge/discharge testing was conducted in the voltage range of 0.01-3.0 V (vs. Na/Na^+) using a NEWARE multichannel battery test system.

Supporting Information

Supporting Information is available from the Wiley Online Library or from the author.

Acknowledgements

This work was financially supported by Australian Research Council (ARC) DECRA Grant (DE160100596). Y.Z. Jiang acknowledges support from the National Natural Science Foundation of China (Grant No. 21373184) and the Public Projects of Zhejiang Province (2015C31039).

Received: ((will be filled in by the editorial staff))
Revised: ((will be filled in by the editorial staff))
Published online: ((will be filled in by the editorial staff))

References

[1] S.-W. Kim, D.-H. Seo, X. Ma, G. Ceder, K. Kang, *Adv. Energy Mater.* **2012**, 2, 710.
[2] H. Pan, Y.-S. Hu, L. Chen, *Energy Environ. Sci.* **2013**, 6, 2338.
[3] M. D. Slater, D. Kim, E. Lee, C. S. Johnson, *Adv. Funct. Mater.* **2013**, 23, 947.
[4] N. Yabuuchi, K. Kubota, M. Dahbi, S. Komaba, *Chem. Rev.* **2014**, 114, 11636.
[5] H.-G. Wang, S. Yuan, D.-L. Ma, X.-B. Zhang, J.-M. Yan, *Energy Environ. Sci.* **2015**, 8, 1660.
[6] Y. Wang, L. Mu, J. Liu, Z. Yang, X. Yu, L. Gu, Y.-S. Hu, H. Li, X.-Q. Yang, L. Chen, X. Huang, *Adv. Energy Mater.* **2015**, 5, 1501005.
[7] S. M. Oh, S. T. Myung, C. S. Yoon, J. Lu, J. Hassoun, B. Scrosati, K. Amine, Y. K. Sun, *Nano Lett.* **2014**, 14, 1620.
[8] E. Lee, D. E. Brown, E. E. Alp, Y. Ren, J. Lu, J.-J. Woo, C. S. Johnson, *Chem. Mater.* **2015**, 27, 6755.
[9] D. Yuan, W. He, F. Pei, F. Wu, Y. Wu, J. Qian, Y. Cao, X. Ai, H. Yang, *J. Mater. Chem. A* **2013**, 1, 3895.
[10] S. Yuan, Y.-B. Liu, D. Xu, D.-L. Ma, S. Wang, X.-H. Yang, Z.-Y. Cao, X.-B. Zhang, *Adv. Sci.* **2015**, 2, 1400018.
[11] H. Kim, G. Yoon, I. Park, K.-Y. Park, B. Lee, J. Kim, Y.-U. Park, S.-K. Jung, H.-D. Lim, D. Ahn, S. Lee, K. Kang, *Energy Environ. Sci.* **2015**, 8, 3325.
[12] B. Lin, S. Zhang, C. Deng, *J. Mater. Chem. A* **2016**, 4, 2550.
[13] C. S. Park, H. Kim, R. A. Shakoor, E. Yang, S. Y. Lim, R. Kahraman, Y. Jung, J. W. Choi, *J. Am. Chem. Soc.* **2013**, 135, 2787.
[14] C. Zhu, K. Song, P. A. van Aken, J. Maier, Y. Yu, *Nano Lett.* **2014**, 14, 2175.
[15] Y. You, X.-L. Wu, Y.-X. Yin, Y.-G. Guo, *Energy Environ. Sci.* **2014**, 7, 1643.
[16] W.-J. Li, S.-L. Chou, J.-Z. Wang, Y.-M. Kang, J.-L. Wang, Y. Liu, Q.-F. Gu, H.-K. Liu, S.-X. Dou, *Chem. Mater.* **2015**, 27, 1997.
[17] S. Yu, Y. Li, Y. Lu, B. Xu, Q. Wang, M. Yan, Y. Jiang, *J. Power Sources* **2015**, 275, 45.
[18] X. Xiang, K. Zhang, J. Chen, *Adv. Mater.* **2015**, 27, 5343.
[19] H. Kang, Y. Liu, K. Cao, Y. Zhao, L. Jiao, Y. Wang, H. Yuan, *J. Mater. Chem. A* **2015**, 3, 17899.
[20] H. Hou, C. E. Banks, M. Jing, Y. Zhang, X. Ji, *Adv. Mater.* **2015**, 27, 7861.
[21] Z. Jian, Z. Xing, C. Bommier, Z. Li, X. Ji, *Adv. Energy Mater.* **2016**, 6, 1501874.
[22] Y. S. Yun, Y.-U. Park, S.-J. Chang, B. H. Kim, J. Choi, J. Wang, D. Zhang, P. V. Braun, H.-J. Jin, K. Kang, *Carbon* **2016**, 99, 658.
[23] D. Xu, C. Chen, J. Xie, B. Zhang, L. Miao, J. Cai, Y. Huang, L. Zhang, *Adv. Energy Mater.* **2016**, 6, 1501929.
[24] W. Li, L. Zeng, Z. Yang, L. Gu, J. Wang, X. Liu, J. Cheng, Y. Yu, *Nanoscale* **2014**, 6, 693.
[25] T. Yang, T. Qian, M. Wang, X. Shen, N. Xu, Z. Sun, C. Yan, *Adv. Mater.* **2016**, 28, 539.
[26] X. Leng, S. Wei, Z. Jiang, J. Lian, G. Wang, Q. Jiang, *Sci. Rep.* **2015**, 5, 16629.
[27] W. Sun, X. Rui, J. Zhu, L. Yu, Y. Zhang, Z. Xu, S. Madhavi, Q. Yan, *J. Power Sources* **2015**, 274, 755.
[28] Y. Jiang, M. Hu, D. Zhang, T. Yuan, W. Sun, B. Xu, M. Yan, *Nano Energy* **2014**, 5, 60.
[29] J.-Y. Hwang, S.-T. Myung, J.-H. Lee, A. Abouimrane, I. Belharouak, Y.-K. Sun, *Nano Energy* **2015**, 16, 218.
[30] S. Yuan, X. L. Huang, D. L. Ma, H. G. Wang, F. Z. Meng, X. B. Zhang, *Adv. Mater.* **2014**, 26, 2273.
[31] Y. Zhao, A. Manthiram, *Chem. Mater.* **2015**, 27, 3096.
[32] X. Xie, K. Kretschmer, J. Zhang, B. Sun, D. Su, G. Wang, *Nano Energy* **2015**, 13, 208.
[33] L. Ji, W. Zhou, V. Chabot, A. Yu, X. Xiao, *ACS Appl. Mater. Interfaces* **2015**, 7, 24895.

[34] J. Liu, Y. Wen, P. A. van Aken, J. Maier, Y. Yu, *Nano Lett.* **2014**, 14, 6387.
[35] B. Qu, C. Ma, G. Ji, C. Xu, J. Xu, Y. S. Meng, T. Wang, J. Y. Lee, *Adv. Mater.* **2014**, 26, 3854.
[36] S. Peng, X. Han, L. Li, Z. Zhu, F. Cheng, M. Srinivansan, S. Adams, S. Ramakrishna, *Small* **2016**, 12, 1359.
[37] Y. Zhao, A. Manthiram, *Chem. Mater.* **2015**, 27, 6139.
[38] Z. Hu, Z. Zhu, F. Cheng, K. Zhang, J. Wang, C. Chen, J. Chen, *Energy Environ. Sci.* **2015**, 8, 1309.
[39] L. David, R. Bhandavat, U. Barrera, G. Singh, *Sci. Rep.* **2015**, 5, 9792.
[40] X.-Y. Yu, L. Yu, L. Shen, X. Song, H. Chen, X. W. D. Lou, *Adv. Funct. Mater.* **2014**, 24, 7440.
[41] J. Xiao, L. Wan, S. Yang, F. Xiao, S. Wang, *Nano Lett.* **2014**, 14, 831.
[42] C. Wu, J. Maier, Y. Yu, *Adv. Mater.* **2016**, 28, 174.
[43] C. Zhu, X. Mu, P. A. van Aken, J. Maier, Y. Yu, *Adv. Energy Mater.* **2015**, 5, 1401170.
[44] C. Xing, D. Zhang, K. Cao, S. Zhao, X. Wang, H. Qin, J. Liu, Y. Jiang, L. Meng, *J. Mater. Chem. A* **2015**, 3, 8742.
[45] Y. Zhang, P. Zhu, L. Huang, J. Xie, S. Zhang, G. Cao, X. Zhao, *Adv. Funct. Mater.* **2015**, 25, 481.
[46] T. Zhou, W. K. Pang, C. Zhang, J. Yang, Z. Chen, H. K. Liu, Z. Guo, *Acs Nano* **2014**, 8, 8323.
[47] W. Sun, X. Rui, D. Yang, Z. Sun, B. Li, W. Zhang, Y. Zong, S. Madhavi, S. Dou, Q. Yan, *Acs Nano* **2015**, 9, 11371.
[48] X. Xie, Z. Ao, D. Su, J. Zhang, G. Wang, *Adv. Funct. Mater.* **2015**, 25, 1393.
[49] X. Xie, T. Makaryan, M. Zhao, K. L. Van Aken, Y. Gogotsi, G. Wang, *Adv. Energy Mater.* **2016**, 6, 1502161.
[50] L. David, R. Bhandavat, G. Singh, *Acs Nano* **2014**, 8, 1759.
[51] Q. Zhou, L. Liu, G. Guo, Z. Yan, J. Tan, Z. Huang, X. Chen, X. Wang, *RSC Adv.* **2015**, 5, 71644.
[52] Z. Shadike, M.-H. Cao, F. Ding, L. Sang, Z.-W. Fu, *Chem. Commun.* **2015**, 51, 10486.
[53] X. Liu, K. Zhang, K. Lei, F. Li, Z. Tao, J. Chen, *Nano Research* **2016**, 9, 198.
[54] M. Walter, T. Zuend, M. V. Kovalenko, *Nanoscale* **2015**, 7, 9158.
[55] C. Zhai, N. Du, H. Z. Yang, *Chem. Commun.* **2011**, 47, 1270.
[56] X. W. Lou, C. M. Li, L. A. Archer, *Adv. Mater.* **2009**, 21, 2536.
[57] Y. Jiang, D. Zhang, Y. Li, T. Yuan, N. Bahlawane, C. Liang, W. Sun, Y. Lu, M. Yan, *Nano Energy* **2014**, 4, 23.
[58] X. Guan, L. Li, G. Li, Z. Fu, J. Zheng, T. Yan, *J. Alloy. Comp.* **2011**, 509, 3367.
[59] L. Zhang, H. B. Wu, S. Madhavi, H. H. Hng, X. W. Lou, *J. Am. Chem. Soc.* **2012**, 134, 17388.
[60] X. Wang, X.-L. Wu, Y.-G. Guo, Y. Zhong, X. Cao, Y. Ma, J. Yao, *Adv. Funct. Mater.* **2010**, 20, 1680.
[61] H. Wang, D. Ma, X. Huang, Y. Huang, X. Zhang, *Sci. Rep.* **2012**, 2, 701.
[62] H. Geng, S. F. Kong, Y. Wang, *J. Mater. Chem. A* **2014**, 2, 15152.
[63] Z. Wang, X. Li, Y. Yang, Y. Cui, H. Pan, Z. Wang, B. Chen, G. Qian, *J. Mater. Chem. A* **2014**, 2, 7912.
[64] N. Mahmood, C. Z. Zhang, Y. L. Hou, *Small* **2013**, 9, 1321.
[65] T. S. Wang, P. Hu, C. J. Zhang, H. P. Du, Z. H. Zhang, X. G. Wang, S. G. Chen, J. W. Xiong, G. L. Cui, *ACS Appl. Mater. Interfaces* **2016**, 8, 7811.
[66] Q. Pan, J. Xie, T. Zhu, G. Cao, X. Zhao, S. Zhang, *Inorg. Chem.* **2014**, 53, 3511.
[67] W. Ma, Y. Guo, X. Liu, D. Zhang, T. Liu, R. Ma, K. Zhou, G. Qiu, *Chem. Eur. J* **2013**, 19, 15467.
[68] R. Jasinski, B. Burrows, *J. Electrochem. Soc.* **1969**, 116, 422.

[69] S.-C. Han, K.-W. Kim, H.-J. Ahn, J.-H. Ahn, J.-Y. Lee, *J. Alloy. Comp.* **2003**, 361, 247.
[70] J. Vetter, P. Novák, M. R. Wagner, C. Veit, K. C. Möller, J. O. Besenhard, M. Winter, M. Wohlfahrt-Mehrens, C. Vogler, A. Hammouche, *J. Power Sources* **2005**, 147, 269.
[71] M. Dahbi, N. Yabuuchi, K. Kubota, K. Tokiwa, S. Komaba, *Phys. Chem. Chem. Phys.* **2014**, 16, 15007.
[72] G. D. Park, J. S. Cho, Y. C. Kang, *Nanoscale* **2015**, 7, 16781.

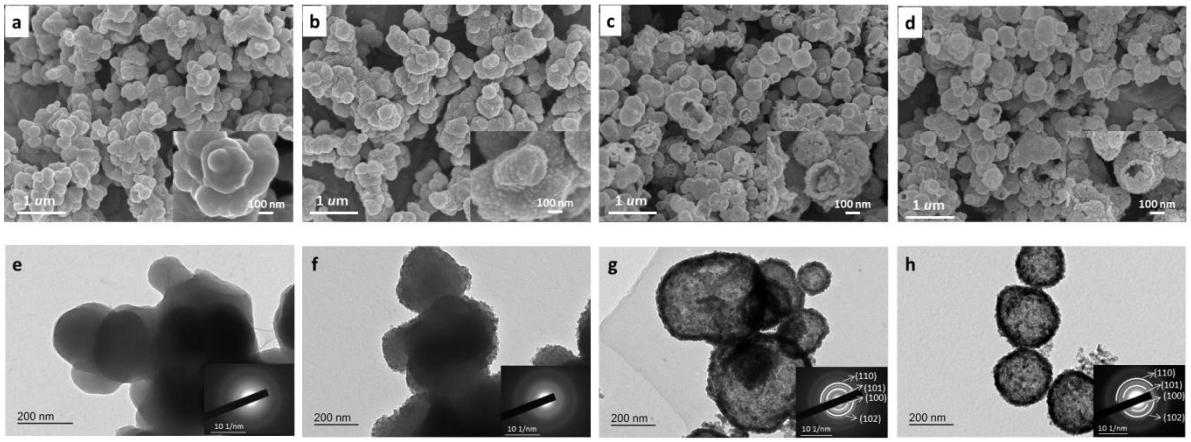

Figure 1. SEM images of NiS synthesized at different temperatures: a) 180 ºC; b) 200 ºC; c) 220 ºC; d) 240 ºC. The insets in panels a-d are the corresponding high-magnification SEM images. TEM images of NiS synthesized at different temperatures: e) 180 ºC; f) 200 ºC; g) 220 ºC; h) 240 ºC. The insets in panels e-h are the corresponding SAED patterns.

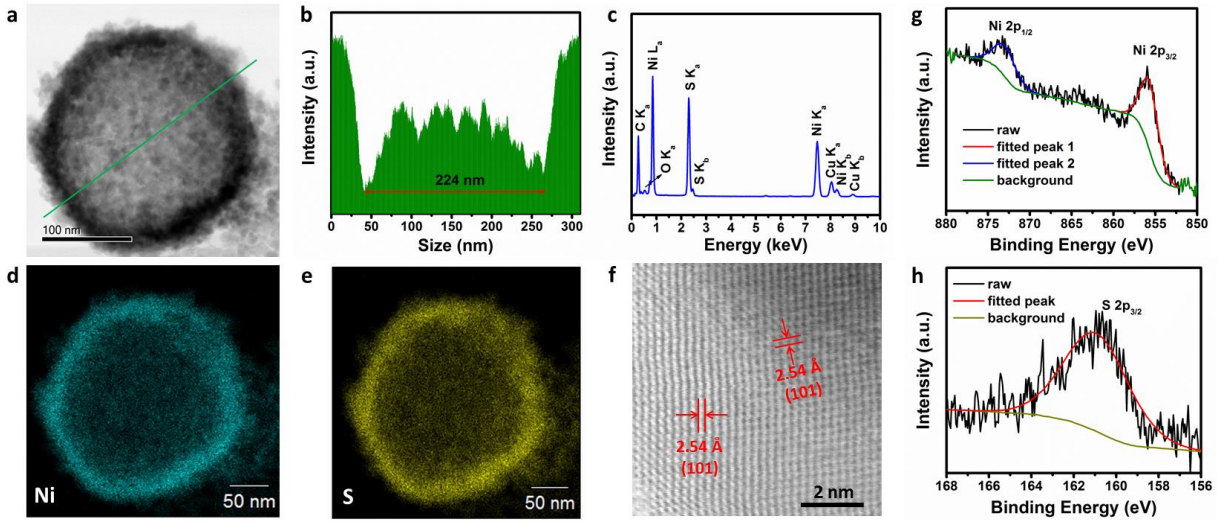

Figure 2. a) High magnification TEM image of NS240; b) electron signal counts from the cross-section of the hollow NiS sphere marked in (a); c) EDX spectrum of NS240; Corresponding EDX elemental mappings of hollow sphere in (a): d) Ni and e) S; f) HRTEM image of NS240; XPS spectra of g) Ni and h) S for NS240.

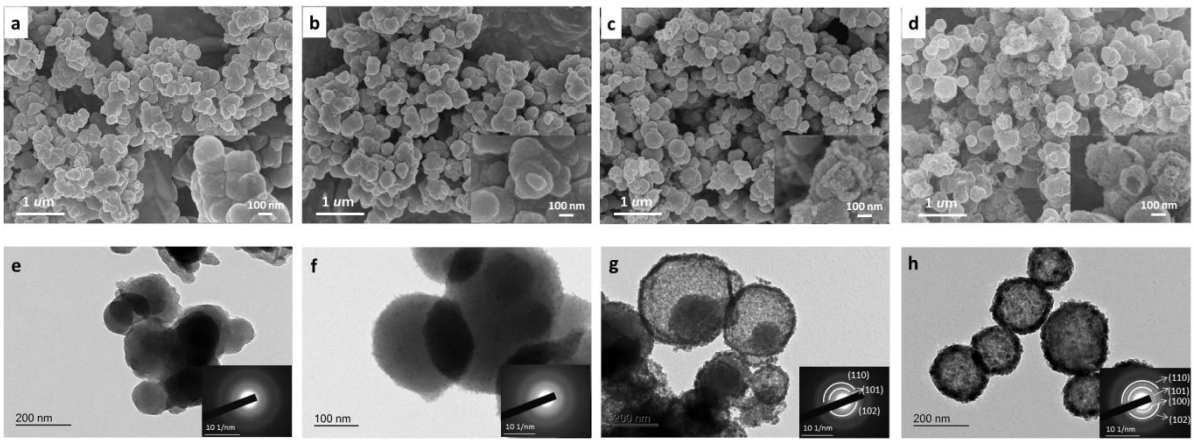

Figure 3. SEM images of NiS prepared at 220 ^{o}C with different reaction times: a) 1 min, b) 10 min, c) 30 min; d) 4 h. The insets in panels a-d are the corresponding high-magnification SEM images. TEM images of NiS prepared at 220 ^{o}C with different reaction times: e) 1 min, f) 10 min, g) 30 min; h) 4 h. The insets in panels e-h are the corresponding SAED patterns.

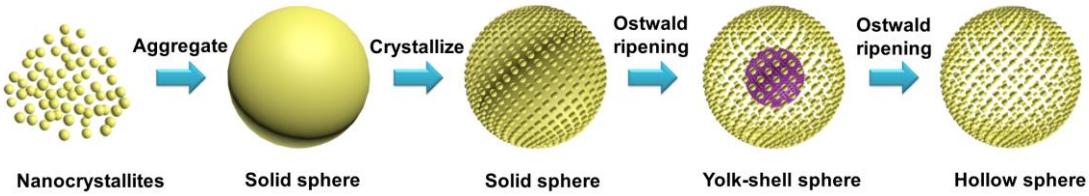

Figure 4. Schematic illustration of the formation mechanism of the hierarchical hollow NiS spheres (with the yellow spheres representing NiS nanoparticles and the purple sphere representing the NiS solid core).

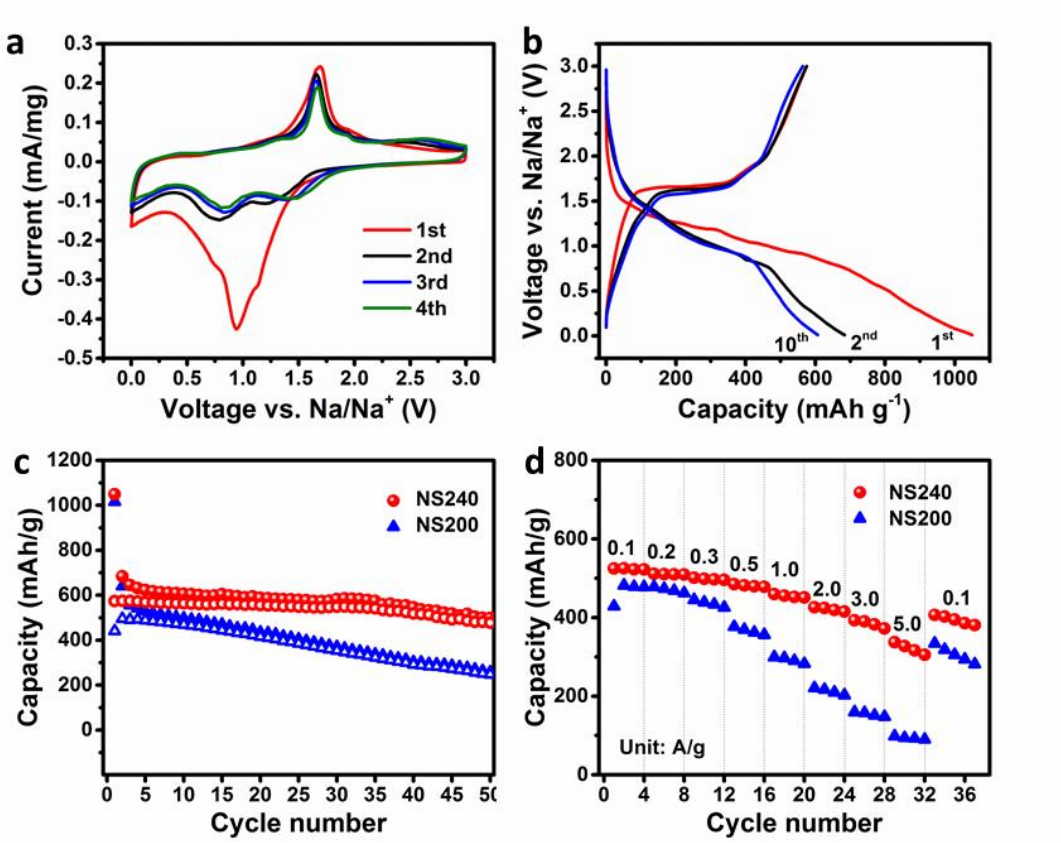

Figure 5. a) CV curves of NS240 electrodes in the voltage window of 0.001-3.0 V at a scan rate of 0.5 mV s^{-1}; b) galvanostatic charge/discharge profiles for the 1st, 2nd, and 10th cycles of NS240 electrodes in the voltage window of 0.01-3.0 V at 100 mA g^{-1}; c) cycling performance of NS240 and NS200 electrodes in the voltage window of 0.01-3.0 V at 100 mA g^{-1}; d) rate capability of NS240 and NS200 electrodes at different current rates in the voltage window of 0.01-3.0 V.

Hierarchical hollow nickel sulfide spheres with porous shells composed of nanoparticles are designed and synthesized, which are shown to be formed by the Ostwald ripening mechanism. As an anode material for SIBs, the NiS spheres deliver high specific capacity, superior cycling stability and rate capability, based on their unique hollow structure, which ensures high Na ion accessibility and strong structural integrity.

Keyword: NiS, hollow structure, anode, sodium-ion batteries

Dan Zhang, Wenping Sun, Yu Zhang, Yuhai Dou, Yinzhu Jiang*, Shixue Dou*

Engineering Hierarchical Hollow Nickel Sulfide Spheres for High-Performance Sodium Storage

ToC figure

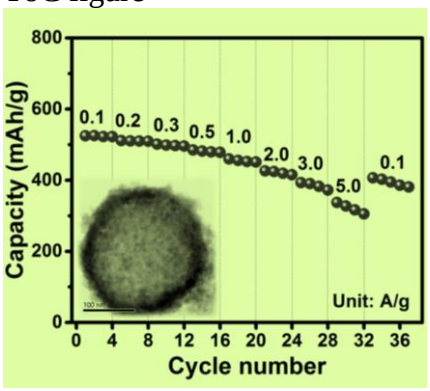

Supporting Information

Engineering Hierarchical Hollow Nickel Sulfide Spheres for High-Performance Sodium Storage

Dan Zhang, Wenping Sun, Yu Zhang, Yuhai Dou, Yinzhu Jiang*, Shixue Dou*

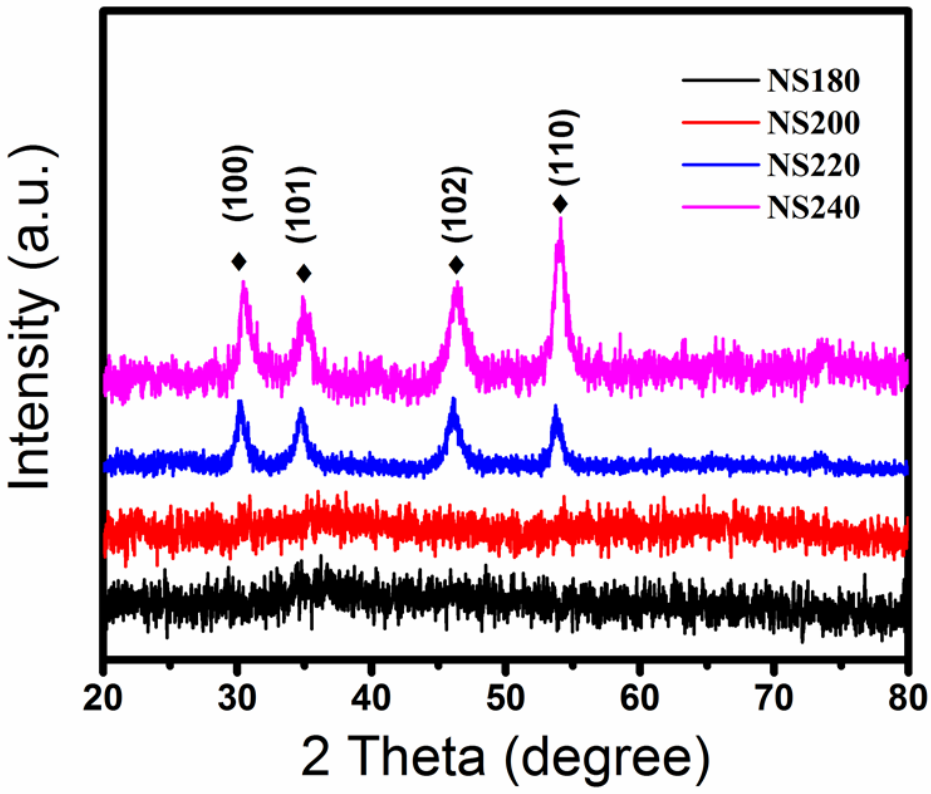

Figure S1 XRD patterns of NiS prepared at different temperatures.

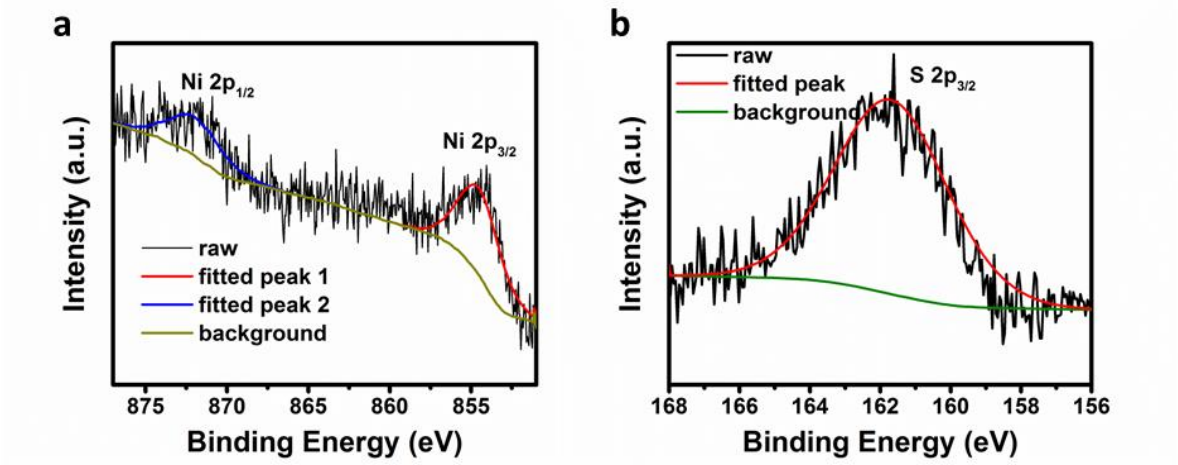

Figure S2 XPS spectra of a) Ni and b) S for NS180.

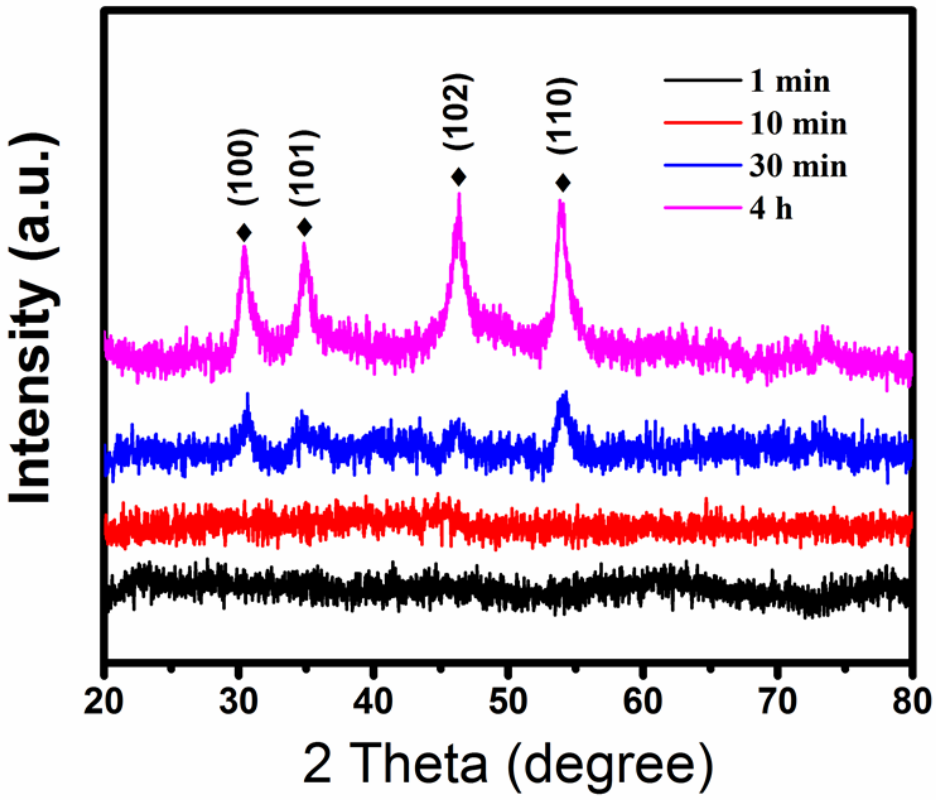

Figure S2 XRD patterns of NiS prepared at 220 ºC with different reaction times.

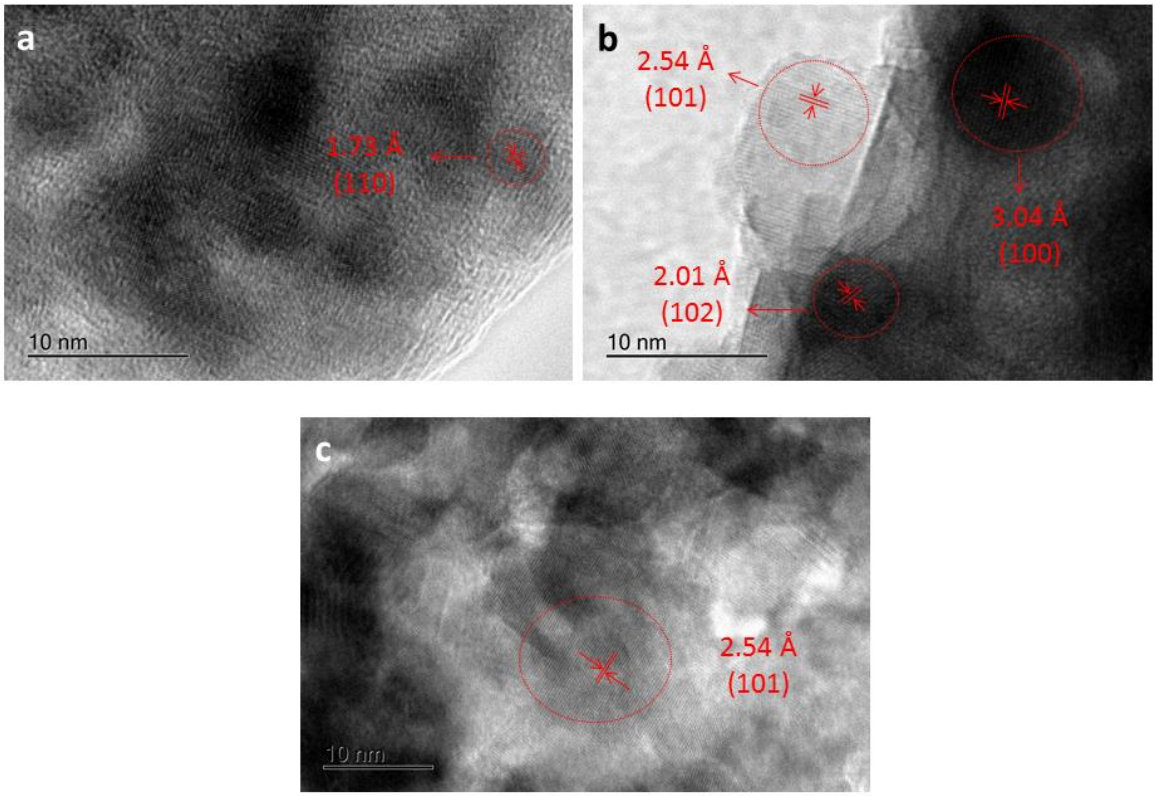

Figure S3 HRTEM images of NiS prepared at 200 °C for 10 min (a), 30 min (b), and 4 h (c).

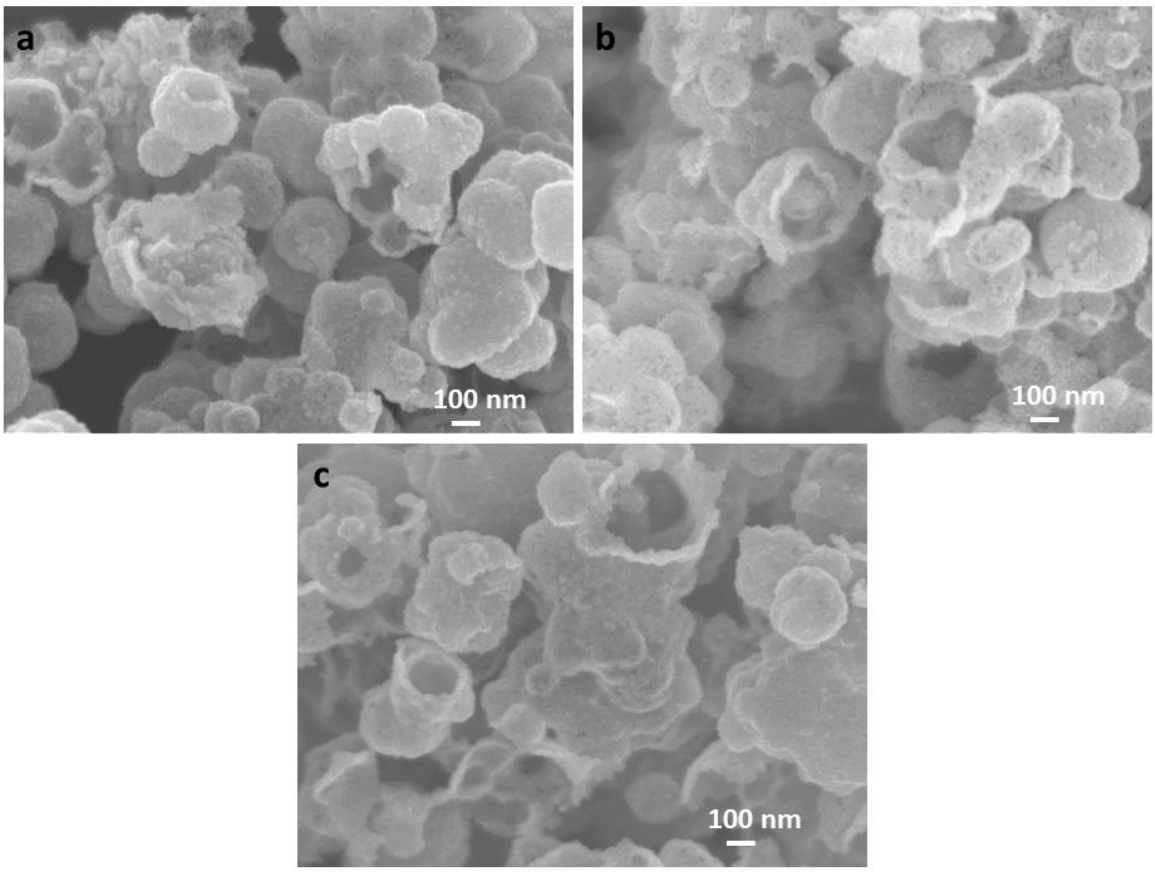

Figure S4 SEM images of NiS prepared at 240 ºC for 5 min (a), 30 min (b) and 2 h (c).

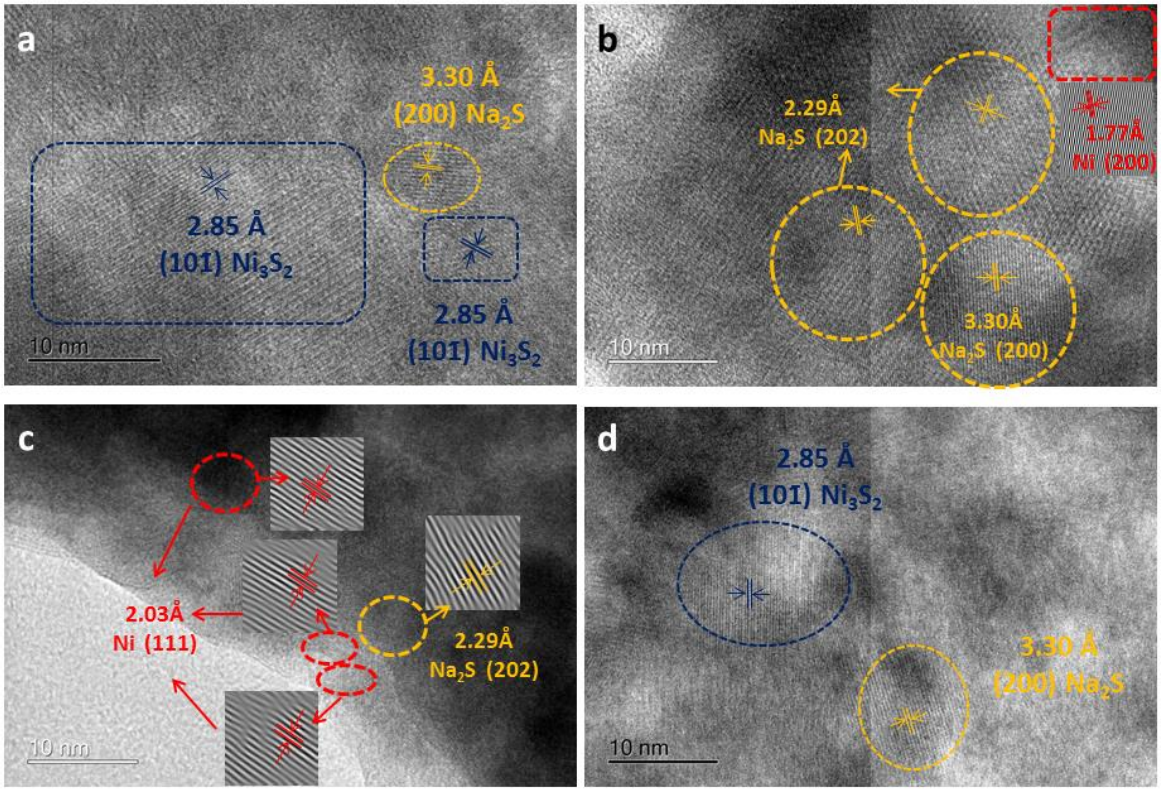

Figure S5 Ex-situ HRTEM images of NS240 electrodes during the first charge-discharge process: (a) 1st discharge to 1.0 V, (b,c) 1st discharge to 0.01 V, and (d) 1st charge to 3.0V. The insets in panel c are corresponding inverse FFT images of selected areas.

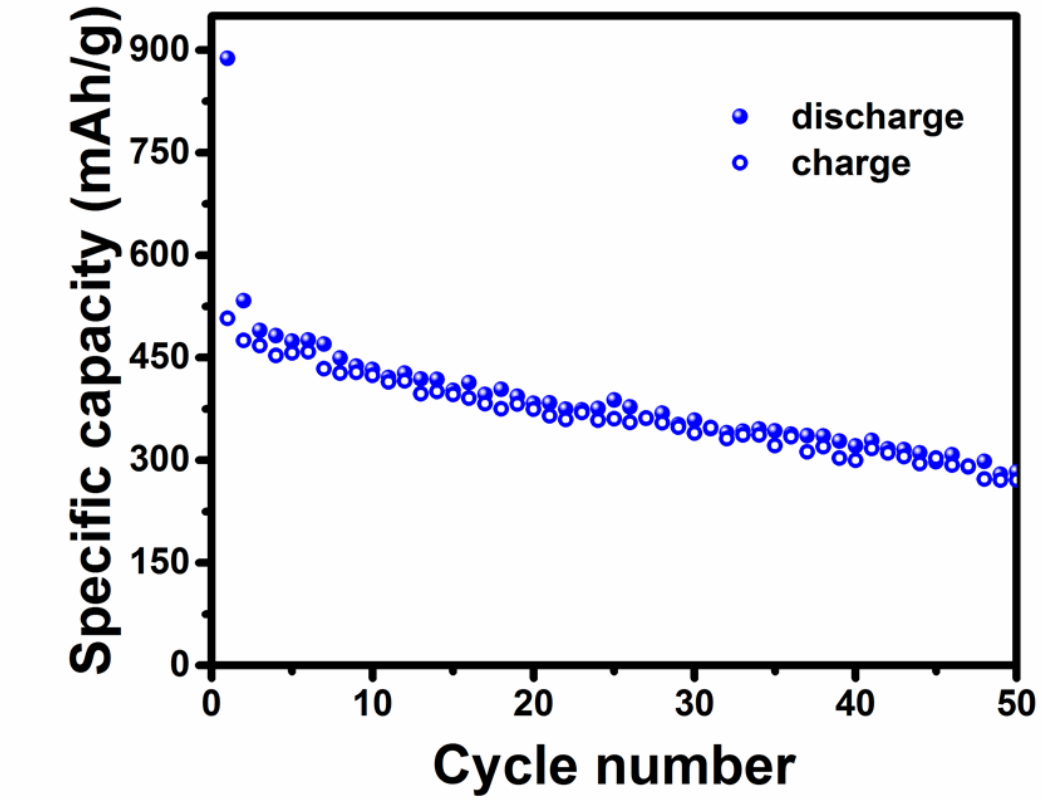

Figure S6 Cycling performance of NS240 electrode in the voltage window of 0.005-3.0 V at 500 mA g^{-1}.

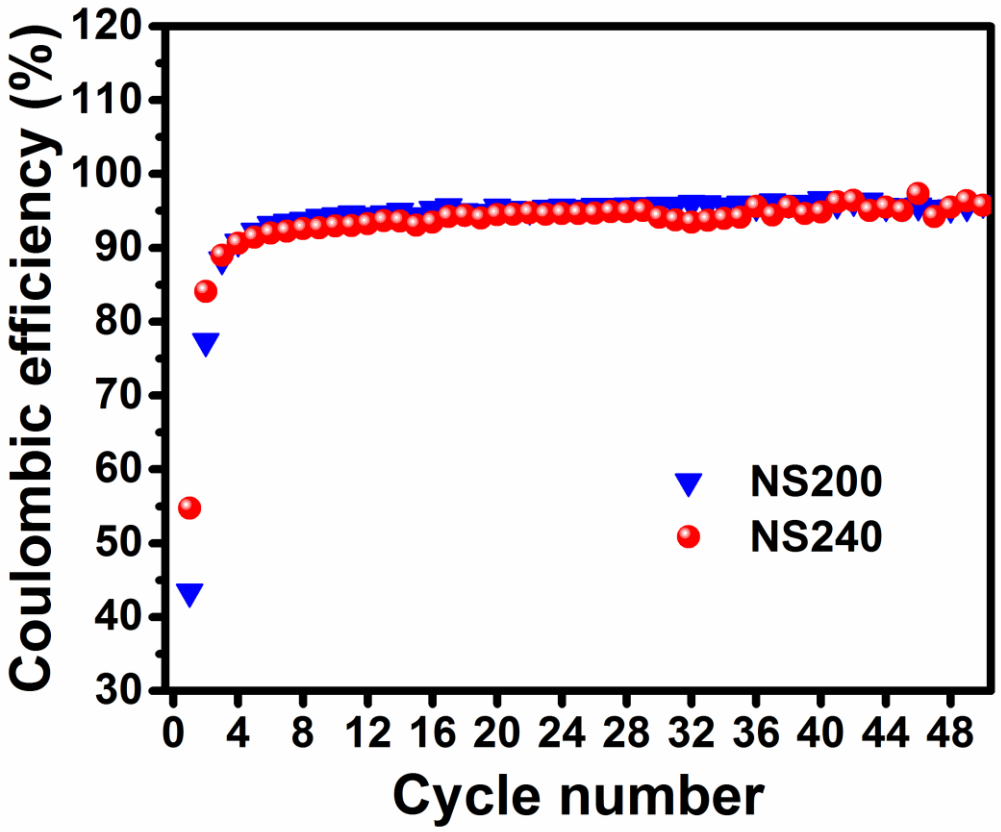

Figure S7 Corresponding coulombic efficiency of all cycles of NS240 and NS200 electrodes in Figure 5c.

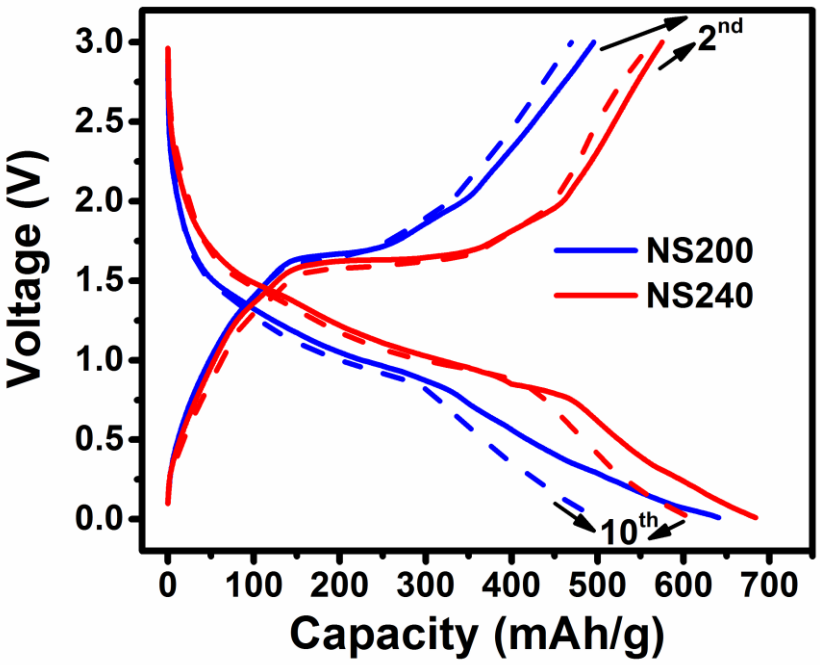

Figure S8 Comparison of charge-discharge curves of NS200 and NS240.

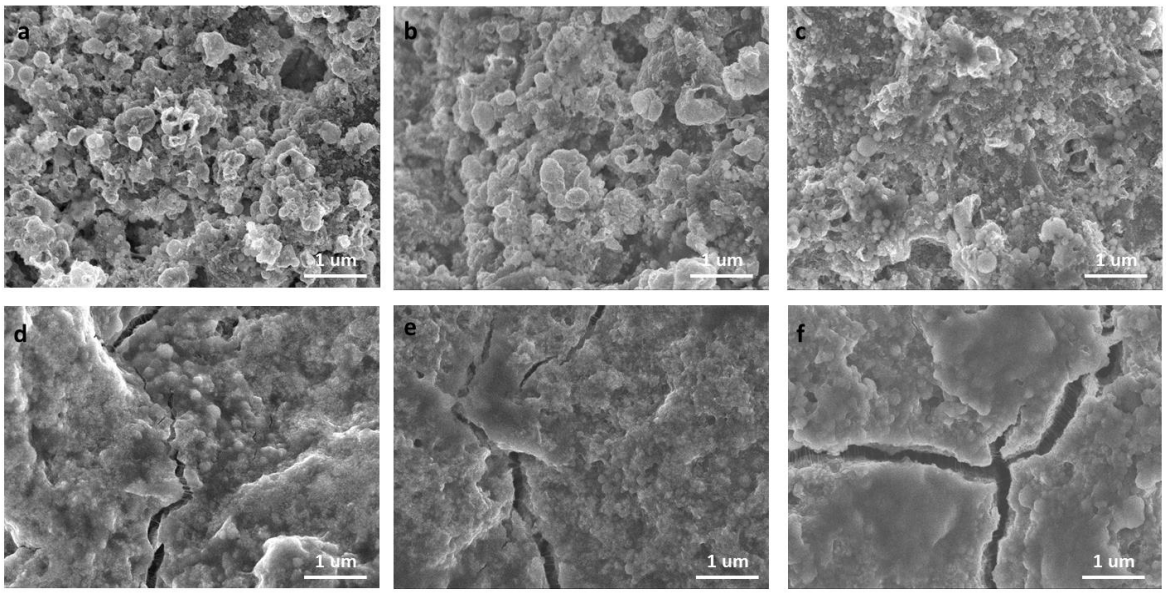

Figure S9 Ex-situ SEM of NiS electrodes after cycling test: NS240 electrodes after 1st cycle (a), 5th cycle (b) and 20th cycle (c); NS200 electrodes after 1st cycle (d), 5th cycle (e) and 20th cycle (f).

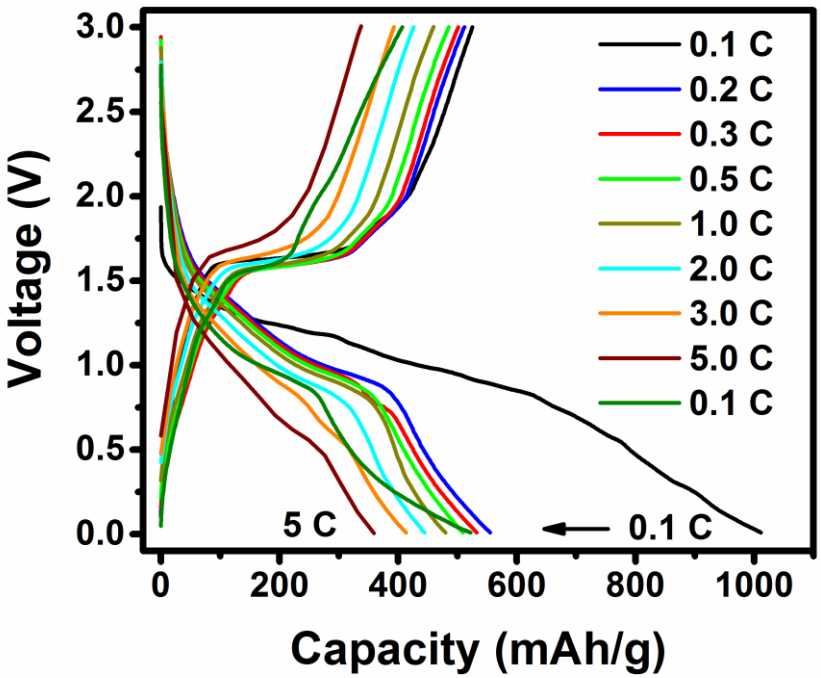

Figure S10 Corresponding charge-discharge curves of initial cycle at different rates in Figure. 5d.

Table S1 Comparison of NS240 electrode with preciously published other nickel sulphides (e.g. β-NiS, NiS_2 and Ni_3S_2) as SIB anodes, in terms of discharge capacity and rate capability.

Electrodes	Cycling capacity/ current density (mAh g^{-1}/ mA g^{-1})		Rate Capability/ current density (mAh g^{-1}/ mA g^{-1})	
	1^{st}	50^{th}		
NS240 (This work)	1049.3/100	499.9/100	393.0 /3000	337.4/5000
β-NiS[66]	513/50	N/A	~180/200	~150/400
β-NiS/ 20rGO[66]	701/50	N/A	181/200	~180/400
NiS_2[65]	~600/80.7	~150/80.7	13/807	9/1614
NiS_2/G[65]	~780/80.7	~400/80.7	221/807	168/1614
Ni_3S_2/rGO[72]	626/300	~449/300	442/1000	411/2000